Morphology of Platinum Electrodeposits in the Three-Dimensional Sublayer to Full Layer Range Produced under Different Potential Modulations on Highly Oriented Pyrolytic Graphite[†]

F. J. Rodríguez Nieto,[‡] M. A. Pasquale,[‡] C. R. Cabrera,[§] and A. J. Arvia*,[‡]

Instituto de Investigaciones Fisicoquímicas Teóricas y Aplicadas (INIFTA), Universidad Nacional de La Plata-Consejo Nacional de Investigaciones Científicas y Técnicas, Sucursal 4, Casilla de Correo 16, 1900 La Plata, Argentina, and Chemistry Department, University of Puerto Rico, Riopiedras, Puerto Rico

The topography of platinum electrodes produced by electrodeposition (19 to 200 mC cm^{-2}) on highly oriented pyrolytic graphite (HOPG) under different potential modulations was investigated by atomic force microscopy, scanning tunneling microscopy, and H-atom electrosorption voltammetry. To modulate electrodeposition, (i) triangular potential cycling at 0.1 V s^{-1}, (ii) a linear cathodic potential at 0.1 V s^{-1} and anodic potential step cycling, and (iii) square wave potential cycling at 5000 Hz were utilized. AFM and STM imaging showed that at lower platinum loading the HOPG surface was partially covered by a 3D sublayer of platinum. Electrodes produced by procedure (i) were made of faceted platinum aggregates of about 200 nm and nanoclusters in the range of 5−20 nm; those that resulted from procedure (ii) consisted of anisotropic aggregates of nanoclusters arranged as quasi-parallel domains. These electrodes from (i) and (ii) behaved as fractal objects. The electrodes resulting from procedure (iii) exhibited a flat surface that behaved as a Euclidean object. For all WEs, as the platinum loading was increased the HOPG surface was fully covered by a thin 3D layer of platinum aggregates produced by electrodeposition and coalescence phenomena. Large platinum loading led to electrodes with fractal geometry. Statistical parameters (root-mean-square height, skewedness, kurtosis, anisotropy, Abbot curve, number of protrusions and valleys, and fractal dimension) were obtained from the analysis of AFM and STM imaging data. Platinum electrodeposition coupled to either H-adatom formation for procedures (i) and (ii) or phonon dispersion for (iii) was involved in the surface atom rearrangements related to electrofaceting. The H-adatom electrosorption voltammetry data were used to evaluate the real electrode surface area via the voltammetric charge and to advance a tentative explanation of the contribution of the different crystallographic facets to the global electrochemical process dominated by weak H−Pt adsorption interactions.

1. Introduction

The design of high-performance electrocatalysts is the result of some combination of surface reactivity, electronic conductivity at electrodes, ionic conductivity, electron−hole pair separation, nature of the support, and facile mass transport of molecules. The fact that in electrochemical reactions the electron is a reactant that scales with the electrified surface area poses the issue of the optimum surface morphology and pore size of electrode material compatible with the highest electrocatalytic activity.[1−5]

Recently, the relevance of nanosize-range metal clusters in an architectural electrode design has been emphasized by paying particular attention to a detailed topographic description, cluster size distribution, shape evolution, and cluster interactions in relation to the electrocatalytic activity of those materials for a number of heterogeneous reactions.[6−11]

A number of physical and chemical procedures have been described to modify the topographic characteristics of solid metal surfaces to produce reproducible and more efficient catalysts.[12−17] One of these procedures involves the application of a periodic electrical perturbation to a metal/conducting environment (either an electrolyte solution or a molten salt) interface. The result of these treatments is either a change in the initial metal topography to develop a preferred crystallographic orientation and surface stepping[12,14] or a change in roughness,[14−17] or both simultaneously. The relative contribution of these effects depends on the appropriate setting of the potential routine (i.e., the potential window, the symmetry and frequency of perturbation and its duration, the environmental composition, the temperature, and the pressure). These procedures furnish reproducible solid

(1) Vielstich, W. *Brennstoffelemente*; Verlag Chemie, GmbH: Weinheim, Germany, 1965.

(2) Bockris J. O'M.; Srinivasan S. *Fuel Cells: Their Electrochemistry*; McGraw-Hill: New York, 1969.

(3) Appleby A. J. In *Proceedings of the Symposium on Electrocatalysis*; Breiter, M., Ed.; Electrochemical Society: Princeton, NJ, 1974.

(4) Lipkowski, J. J. In *Electrocatalysis*; Ross, P. N., Ed.; Wiley-VCH: New York, 1998.

(5) Vielstich, W.; Lamm, A.; Gasteiger, H., Eds. *Handbook of Fuel Cells: Fundamentals, Technology, and Applications*; Wiley: New York, 2003.

(6) Kinoshita, K. *J. Electrochem. Soc.* **1990**, *137*, 845.

(7) Petroski, J. M.; Wang, Z. L.; Green, T. C.; El-Sayed, M. A. *J. Phys. Chem. B* **1998**, *102*, 3316.

(8) Guo, Y.; Guadalupe, A. R. *Langmuir* **1999**, *15*, 759.

(9) Feldheim, D. L.; Foss, C. A., Eds. *Metal Nanoparticles: Synthesis, Characterization, and Applications*; Marcel Dekker: New York, 2002.

(10) Hernández Creus, A.; Gimeno, Y.; Salvarezza, R. C.; Arvia, A. J. In *Encyclopedia of Nanoscience and Nanotechnology: Crystal Engineering of Metallic Nanoparticles*; Nalwa, H. S., Ed.; American Scientific Publishers: New York, 2004; p 221.

(11) Rotello, V. *Nanoparticles: Building Blocks for Nanotechnology.* Kluwer Academic/Plenum Publishers: New York, 2004.

(12) Arvia, A. J.; Canullo, J. C.; Custidiano, E.; Perdriel, C. L.; Triaca, W. E. *Electrochim. Acta* **1986**, *31*, 1368.

(13) Chialvo, A. C.; Triaca, W. E.; Arvia, A. J. J. *Electroanal. Chem.* **1983**, *146*, 93.

(14) Salvarezza, R. C.; Arvia, A. J. In *Modern Aspects of Electrochemistry*; White, R. E., Conway, B. E., Bockris, J. O'M., Eds.; Plenum Press: New York 1996; Vol. 28, Chapter 5, pp 289−373.

(15) Mayrhofer, K. J. J.; Blizanac, B. B.; Arez, M.; Stamenkovic, V. R.; Ross, P. N.; Markovic, N. M. *J. Phys. Chem. B* **2005**, *109*, 14440.

(16) Komanicky, V.; Menzel, A.; You, H. *J. Phys. Chem. B* **2005**, *109*, 23543.

(17) Komanicky, V.; Menzel, A.; Chang, K.-C.; You, H. *J. Phys. Chem. B* **2005**, *109*, 23550.

electrode topography on either a polycrystalline, single crystal, or dispersed metal electrode immersed in either an aqueous or molten electrolyte. Electrodes of a similar type can also be produced by metal electrodeposition under electrical modulation on a well-defined electrochemically inert conducting substrate such as highly oriented pyrolytic graphite (HOPG).[18−20] In this case, metal clusters in the range of 5 to 100 nm with different sizes and shapes, cluster size distributions, and relative distribution of crystallographic facets can be prepared.[12,21,22] Electrodes of this type exhibited an enhancement of their electrocatalytic properties for a number of reactions of technical interest.[23−29]

Platinum metals and a number of their alloys with other transition metals are of particular interest as electrocatalysts to be utilized as dispersed metals in different carbon materials and in power sources for stationary and vehicle applications.[30−33] The structure of these electrodes consists of ultrathin coatings of platinum on the carbon support with different Pt/C weight ratios or dispersed platinum as nano- or mesoparticles. In all cases, the particle morphology greatly depends on the preparation procedure. However, despite the advances that have been made in the past decades in the handling and modeling of single-crystal surfaces[34−36] there is no conclusive answer yet to validate the models for the crystallography of these particles and their roughness characteristics at the interfaces.

The motivation of this work was to investigate the topography of clean platinum 3D aggregates at the submonolayer and thin layer thickness on highly oriented pyrolytic graphite immersed in aqueous sulfuric acid. The platinum layers were prepared by electrodeposition under modulation by different potential routines.[14] The electrode topography was imaged utilizing AFM and STM techniques, and the distribution of crystallographic facets was determined by X-ray diffraction (XRD) patterns. The voltammetric response of the H-atom electrosorption processes was also determined. The statistical parameters derived from the cross-section analysis of AFM and STM images provided quantitative information about the roughness of different platinum overlayers on HOPG. XRD patterns and electrochemical data
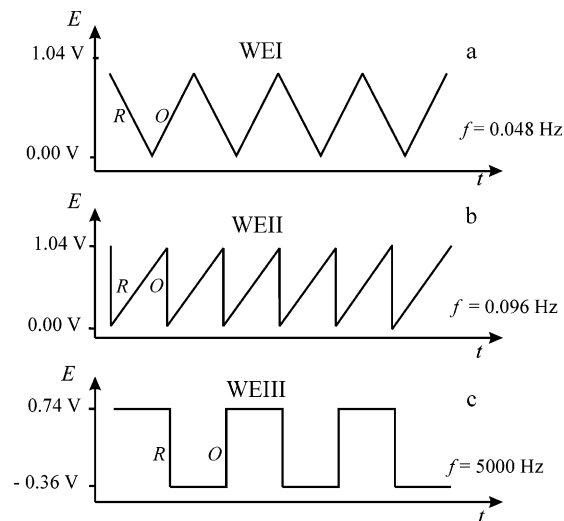

Figure 1. Schemes of the superimposed potential routines, including switching potentials and frequency values, utilized in the electrochemical preparation of HOPG/platinum electrodes WEI, WEII, and WEIII. R and O stand for the modulating signal electro-reduction and electro-oxidation half-cycles, respectively.

indicate that the trend toward electrofaceting involves the preferred development of platinum facets exhibiting a weak interaction with H-adatoms. These results should contribute to providing fundamental aspects of the surface topography of platinum at platinum/HOPG interfaces and its modification by potential modulation techniques. This information can be useful for the design of platinum/carbon interfaces for a diversity of electrochemical cells.

2. Experimental Section

2.1. Working Electrode Preparation. The working electrodes (WEs) consisted of a 1×1 cm^2 surface of the basal plane of highly oriented pyrolytic graphite (HOPG) (SP1 from Structure Probe, Inc) that was freshly cleaved utilizing the adhesive tape technique. The HOPG surface was covered either partially or completely with a platinum layer that was electrodeposited from nitrogen-purged aqueous 1.0 M sulfuric acid + ($5.0 \times 10^{-3} \leq x \leq 1.0 \times 10^{-2}$ M) potassium hexachloroplatinate. Platinum electrodeposition was made at room temperature under cyclic potential routines utilizing (i) a triangular; (ii) a saw-tooth, and (iii) a square wave potential perturbation (Figure 1) covering the potential window ($\Delta E = E_u - E_l$), potential scanning rate (v), and frequency (f). These WEs are hereafter referred to as WEI, WEII, and WEIII, respectively. The potential routines were selected from data of previous work on the electrochemical faceting of polycrystalline platinum with the condition that $\Delta E/2$ was lower than the reversible potential of the [PtCl$_6$]$^{2-}$/[PtCl$_4$]$^{2-}$ ($E° = 0.68$ V) and [PtCl$_4$]$^{2-}$/[Pt^0] ($E° = 0.755$ V) redox couples[37] to avoid potential modulation-assisted platinum electrodissolution. The platinum loading was expressed as the electrodeposition charge density (q_{Pt}) for 100% Coulombic efficiency as mC cm^{-2} HOPG. The specific WE surface area on the nanoscale (A_H) was determined from the H-adatom voltammetric charge.[38]

A three-electrode glass cell consisting of an O-ring joint for mounting each WE (cathode) with 0.26 cm^2 exposed circular area was used. A platinum wire mesh (anode) and a saturated calomel electrode (SCE) with a Luggin−Haber capillary tip arrangement were utilized as the auxiliary electrode and reference electrode, respectively. Potentials in the text are reported on the normal hydrogen electrode (NHE) scale.

A potentiostat (EG&G Princeton Applied Research, models 263-A and 273-A) with either M-270 software or coupled to an $x-y$ recorder

(18) Martin, H.; Hernández Creus, A.; Carro, P.; González, S.; Salvarezza, R. C.; Arvia, A. J. *J. Phys. Chem.* **1999**, *106*, 3900.

(19) Martin, H.; Hernández Creus, A.; Andreasen, G.; Salvarezza, R. C.; Arvia, A. J. *Langmuir* **2000**, *16*, 2915.

(20) Gimeno, Y.; Hernández Creus, A.; Carro, P.; González, S.; Salvarezza, R. C.; Arvia, A. J. *J. Phys. Chem. B* **2002**, *106*, 4232.

(21) Canullo, J. C.; Triaca, W. E.; Arvia, A. J. *J. Electroanal. Chem.* **1984**, *175*, 337.

(22) Cerviño, R. M.; Triaca, W. E.; Arvia, A. J. *J. Electroanal. Chem.* **1985**, *182*, 51.

(23) Cerviño, R. M.; Triaca, W. E.; Arvia, A. J. *J. Electroanal. Chem.* **1985**, *132*, 266.

(24) Triaca, W. E.; Kessler, T.; Canullo, J. C.; Arvia, A. J. *J. Electrochem. Soc.* **1987**, *134*, 67.

(25) Marcos, M. L.; Vara, J. M.; González-Velasco, J.; Arvia, A. J. *J. Electroanal. Chem.* **1987**, *224*, 189.

(26) Visintin, A.; Canullo, J. C.; Triaca, W. E.; Arvia, A. J. *J. Electroanal. Chem.* **1988**, *239*, 67.

(27) Castro Luna, A. M.; Giordano, M. C.; Arvia, A. J. *J. Electroanal. Chem.* **1989**, *259*, 173.

(28) Beden, B.; Hahn, F.; Léger, J. M.; Lamy, C.; Perdriel, C. L.; Tacconi, N. R. De; Lezna, R. O.; Arvia, A. J. *J. Electroanal. Chem.* **1991**, *301*, 129.

(29) Martins, M. E.; Salvarezza, R. C.; Arvia, A. J. *Electrochim. Acta* **1991**, *36*, 1617.

(30) Mukerjee, S.; Srinivasan, S.; Soriaga, M. P.; McBreen, J. *J. Phys. Chem.* **1995**, *99*, 4577.

(31) Cho, J.; Roh, D.-K.; Yoon, J.-B.; Choy, J.-H.; Kim, H. *J. Chem. Soc., Faraday Trans.* **1998**, *94*, 2835.

(32) Shukla, A. K.; Neergat, M.; Bera, P.; Jayaran, V.; Hegde, M. S. *J. Electroanal. Chem.* **2001**, *504*, 111.

(33) Antonili, E.; Passos, R. R.; Ticianelli, R. A. *Electrochim. Acta* **2002**, *48*, 263.

(34) Clavilier, J.; Fauré, R.; Guinet, G.; Durand, R. *J. Electroanal. Chem.* **1980**, *107*, 205.

(35) Furuya, N.; Koide, S. *Surf. Sci.* **1989**, *220*, 18.

(36) Itaya, K. *Prog. Surf. Sci.* **1998**, *58*, 123.

(37) Lide, D. R., Ed. *CRC Handbook of Chemistry and Physics,* 86th ed.; Taylor & Francis: London, 2005.

(38) Conway, B. E. *Prog. Surf. Sci.* **1995**, *49*, 331.

(SOLTEC-VP-6415S) and a wavefunction generator (Hewlett-Packard, 8116A pulse/function generator) were utilized. Runs were made at room temperature.

2.2. Topography of WEs. The reproducibility of the HOPG surface was checked either after fresh cleavage of the HOPG surface or when cleavage was followed by slight rubbing with a smooth paper tissue. The latter provided an improved visual aspect of the surface by conventional microscopy. Besides, the reproducibility of HOPG substrates of different stocks from the same supplier was also verified. In this case, it was found that the initial amount of electrodeposited platinum predicted for preset working conditions could be utilized as a direct indication of the density number of nucleation sites for platinum attachment. Therefore, only those WEs for which the difference between the actual and the expected amount of electrodeposited platinum was within a few percent were utilized.

After platinum electrodeposition, each WE was removed from the cell at 0.5 V, rinsed with distilled water, and dried under nitrogen. Subsequently, its topography was investigated by atomic force microscopy (AFM) and scanning tunneling microscopy (STM) utilizing NanoScope IIIa and NanoScope III instruments, respectively (Digital Instruments, Santa Barbara, CA).

For contact mode AFM imaging, a silicon nitride probe with a 0.06 N m^{-1} spring constant was employed. For constant-current mode STM imaging, 80:20 platinum–iridium tips under bias voltages in the range of $0.03-0.10$ V and tunneling current in the range of $1-3$ nA were used. The quality of these tips was tested by atomic resolution imaging of the basal plane of graphite. All measurements were performed in air. The image analysis was carried out with the scanning probe image processor SPIP (Image Metrology, Copenhagen, Denmark), which provided the cross section and grain analysis and made surface roughness distinction on the micrometer and nanometer scales possible.

It should be noted that the sensitivity of AFM for the determination of the true baseline (i.e., the true HOPG plane from the cross-section analysis) depends on both the cantilever size and the separation distance between platinum aggregates. According to the design of the measuring device and the values of q_{Pt} involved in this work, the lowest depth from the upper surface to be distinguished by AFM was estimated to be on the order of 30 nm.

The crystallographic features of the WEs were determined by X-ray diffraction patterns. Data were obtained using an XRD-Phillips APD1700 with a Cu Kα radiation source. The $\theta-2\theta$ decoupling Bragg angles were scanned over the range of $30-110°$ with a step of $0.02°$.

2.3. H-Atom Electrosorption Voltammetry at WEs. The voltammetric behavior of the H-atom electro(ad/de)sorption on WEs at 0.050 V s^{-1} in aqueous 1.0 M sulfuric acid was determined. These voltammograms were used to evaluate q_H from the fifth cycle and to determine the charge distribution of weakly and strongly bound H-adatoms on the platinum surface. The real electrode surface area (A_H) was estimated from the value of q_H evaluated in the range of 0 to 0.40 V, considering 0.220 μC cm^{-2} to be the reference charge for the H-adatom monolayer on Pt(111).[34,35] The voltammetric features of H-adatoms on low-index single-crystal platinum faces in acidic solution have been taken from the literature.[39] Electrochemical data were displayed either as the anodic or cathodic current density (j_a or j_c) versus E plots.

Working solutions were prepared from distilled water (Nanopure System, Barnstead), sulfuric acid (Aldrich 99.999%), and high-purity nitrogen.

3. Results

3.1. Surface Characterization of WEs by AFM. The surfaces of WEs on the mesoscale (μm) were characterized by AFM imaging processing. The surface features depend on both the potential routine and the value of q_{Pt} ($19 \leq q_{Pt} \leq 200$ mC cm^{-2}). In the early stages of growth, platinum nuclei are formed at
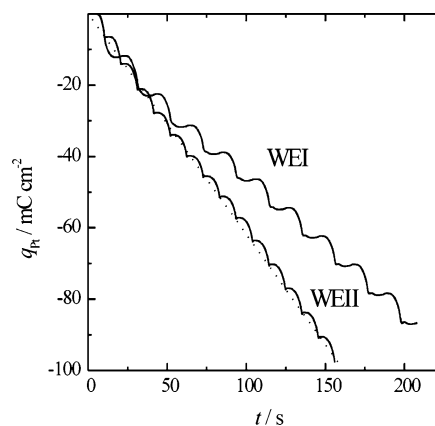

Figure 2. Platinum electrodeposition charge versus electrolysis time plots for the preparation of WEI and WEII. The dashed straight line corresponds to the average charge density $\langle q_{Pt} \rangle$ versus t plot.

HOPG surface defects, particularly at step edges.[40] Further growth implies a dominant platinum-on-platinum surface electrodeposition yielding metal aggregates.[41] As q_{Pt} is increased, aggregates tend to coalesce.

3.1.1. WEI. For WEI preparation, the platinum electrodeposition was run under cyclic triangular potential scanning at 0.100 V s^{-1} in the range of $1.04 \geq E \geq 0.05$ V. The process involves a sequence of electro-oxidation/electro-reduction cycles. For WEI, the q_{Pt} versus time (t) plot deviates from linearity with a decreasing value of d$\langle q_{Pt}\rangle$/dt for $t > 50$ s (Figure 2). This behavior is due to the gradual interference of the H-atom electro-adsorption as E approaches E_l for each cycle. In fact, for WEI preparation the average residence time $\langle \tau \rangle$ of H-adatoms is determined by the time spent by the modulating signal to scan the E_l to the 0.3 V window back and forth. In this case, $\langle \tau \rangle \cong (1/2)(2 \times 0.30$ V/0.10 V s^{-1}) $= 3$ s.

AFM images (10×10 μm^2) for $q_{Pt} = 19$ mC cm^{-2} (Figure 3a) show a nonuniform distribution of rather rounded, egg-shaped top platinum aggregates and partial HOPG surface coverage. Data from the cross-section and grain analyses are assembled in Table 1. The aggregate average height of a few nanometers remains almost constant, irrespective of q_{Pt}. The platinum deposit exhibits an anisotropic roughness as seen from both the cross section analysis in the x and y directions (Figure 3b). The average aspect ratio distribution function of aggregates, defined as the $\langle$length/width$\rangle$ average ratio, exhibits a maximum value at 2.5. AFM images (10×10 μm^2) for $q_{Pt} = 96$ mC cm^{-2} (Figure 3d) show the same type of morphology and an increase in roughness (Figure 3e). In this case, a considerable increase in the HOPG coverage by platinum is obtained. The aspect ratio distribution function (Figure 3f) extends to larger values as q_{Pt} is increased, although the maximum value remains almost constant. These results show that the lower q_{Pt}, the greater the number of aggregates with a small aspect ratio.

3.1.2. WEII. The preparation of WEII platinum electrodeposits was made from aqueous 5×10^{-3} M potassium hexachloro-platinate + 1 M sulfuric acid under a repetitive cycling comprising a linear potential scan at 0.10 V s^{-1} from $E_{as} = 1.04$ V to $E_{cs} = 0$ V, followed by a fast anodic potential step from 0 to 1.04 V. In the first half-cycle, H-adatoms are present for $\langle \tau \rangle \cong 1.5$ s and are almost instantaneously removed in the subsequent half-cycle. In contrast to WEI, for WEII a linear $\langle q_{Pt} \rangle$ versus t plot is obtained (Figure 2) (i.e., $\langle q_{Pt} \rangle$ is proportional to t).

(39) Markovic, N. M.; Grgur, B. N.; Ross, P. N. *J. Phys. Chem. B* **1997**, *101*, 5405.

(40) Zubimendi, J. L.; Vázquez, L.; Ocón, P.; Vara, J. M.; Triaca, W. E.; Salvarezza, R. C.; Arvia, A. J. *J. Phys. Chem.* **1993**, *97*, 5095.
(41) Alonso, C.; Salvarezza, R. C.; Vara, J. M.; Arvia, A. J.; Vázquez, L.; Bartolomé, A.; Baró, A. M. *J. Electrochem. Soc.* **1990**, *137*, 2161.

Figure 3. AFM images (10 × 10 μm^2) of WEI ($q_{Pt} = 19$ mC/cm²) (a) and ($q_{Pt} = 96$ mC/cm²) (d). The corresponding cross-section analysis in the x and y directions is shown in b and e, and aspect ratio distribution functions for the mesoscale topography are depicted in c and f, respectively.

Table 1. Geometric Parameters and Aspect Ratio of Platinum Aggregates and Clusters at WEI, WEII, and WEIII Derived from the Grain Analysis Utilizing AFM and STM Images[a]

	WEI-19	WEI-96	WEII-19	WEII-96	WEII-192	WEIII-19	WEIII-96	WEIII-192
				AFM				
⟨area⟩ nm²	9.37×10^4	8.46×10^4	4.60×10^4	8.47×10^4	3.47×10^5	1.58×10^5	3.21×10^5	2.70×10^4
⟨length⟩ nm	311	459	336	434	710	455	529	183
⟨width⟩ nm	104	131	96	139	250	179	206	60
⟨diameter⟩ nm	200	272	200	274	469	319	369	117
⟨height⟩ nm	92.3	87.6	138	159	285	103	70	108
⟨aspect ratio⟩	2.67	3.34	3.26	2.35	2.64	2.47	2.46	2.65

	WEI-19	WEII-19	WEII-96	WEII-192	WEIII-19
			STM		
⟨length⟩ nm	17.1	9.47	19.4	11.8	6.40
variance (length)	9.1	5.96	6.60	5.40	3.10
⟨width⟩ nm	6.1	8.82	7.50	4.40	2.34
variance (width)	3.7	1.95	2.60	2.20	1.10
⟨aspect ratio⟩	2.98	3.30	2.55	2.68	2.70

[a] The numbers accompanying the WE column headings correspond to the value of q_{Pt} in mC cm⁻².

For $q_{Pt} = 19$ mC cm⁻² (Figure 4a), the electrodeposit consists of irregular aggregates a few nanometers in height and their cross-section analysis and aspect ratio distribution (Figure 4b and c), confirming their anisotropy and dominant growth in the x and y directions (Table 1).

The AFM images from WEII ($q_{Pt} = 96$ mC cm⁻²) (Figure 4d) show the HOPG surface almost completely covered by platinum aggregates with rounded tips that result from the contribution of coalescence phenomena. Likewise, the cross-section analysis (Figure 4e and f), compared to that for $q_{Pt} = 19$ mC cm⁻², indicates a decrease in both the surface anisotropy and roughness due to leveling effects produced by coalescence.

AFM images from WEII for $q_{Pt} = 192$ mC cm⁻² (Figure 4g) show a remarkable contribution of coalescence to the formation of aggregates with parabolic tips (Figure 4h and i). Correspondingly, the cross section and aspect ratio distribution indicate an increase in the electrodeposit isotropy with q_{Pt}, although deep valleys in the topography can still be distinguished. Therefore, for WEII, as q_{Pt} is increased the values of the aspect ratio and number density of aggregates diminish. Aggregate coalescence changes the topography favoring a channel-like surface structure and the isotropy of the electrodeposit.[41,42]

3.1.3. WEIII. The preparation of WEIII with a different q_{Pt} was made by electrodepositing platinum under a periodic square

Figure 4. (a) AFM images ($10 \times 10 \ \mu m^2$) of WEII ($q_{Pt} = 19$ mC/cm²) (a), ($q_{Pt} = 96$ mC/cm²) (d), and ($q_{Pt} = 192$ mC/cm²) (g). The corresponding cross-section analysis in the x and y directions is shown in b, e, and h, and the aspect ratio distribution functions for the meso-scale topography are depicted in c, f, and i, respectively.

wave of $f = 5000$ Hz between $E_u = 0.74$ V and $E_l = -0.36$ V. In this case, the anodic and cathodic processes at E_u and E_l were limited to $\langle \tau \rangle = 5 \times 10^{-4}$ s for each half-cycle. Then, the electroformation of H-adatom and, to some extent, platinum surface atom relaxation processes at longer t were suppressed almost completely.

The AFM images ($10 \times 10 \ \mu m^2$) for $q_{Pt} = 19$ mC cm^{-2} (Figure 5a) show the HOPG surface partially covered by platinum conical islands made of a 3D central core surrounded by smooth aggregates. Otherwise, for $q_{Pt} = 192$ mC cm^{-2} (Figure 5d) a more compact electrodeposit made of small aggregates covers the entire HOPG surface. These electrodeposits exhibit anisotropy (Figure 5b and e) with an almost constant aspect ratio of around 2.5 (Figure 5c and f), irrespective of q_{Pt}.

3.1.4. Data from Roughness Analysis. The following statistical parameters were derived from the roughness analysis of surface imaging utilizing the nomenclature from the software supplier:[43] (i) The root-mean-square height in the z direction, Sq, that measures the width of the height distribution function. The wider the latter, the larger the value of Sq, and the rougher the surface. (ii) The skewedness, Ssk, that describes the asymmetry of the height distribution function. It measures the symmetry of the variation of a profile about its mean line. A positive Ssk indicates fairly high spikes that emerge above the mean line, whereas negative values point out fairly deep valleys in a smoother plateau. (iii) The kurtosis parameter, Sku, that is related to the peakedness of the profile. (iv) The texture parameter, Sti, that measures the anisotropy of the deposit. (v) The height cumulative probability distribution function (Abbott curve) that is characterized by three

(42) Canullo, J. C. *Procesos de Monoorientación Cristalina de Superficies Metálicas.* Doctoral Thesis, Faculty of Exact Sciences, National University of La Plata, La Plata, Argentina, 1993.

(43) *The Scanning Probe Image Processor SPIP User's and Reference Guide*, version 4; Image Metrology: Copenhagen, Denmark, 2005.
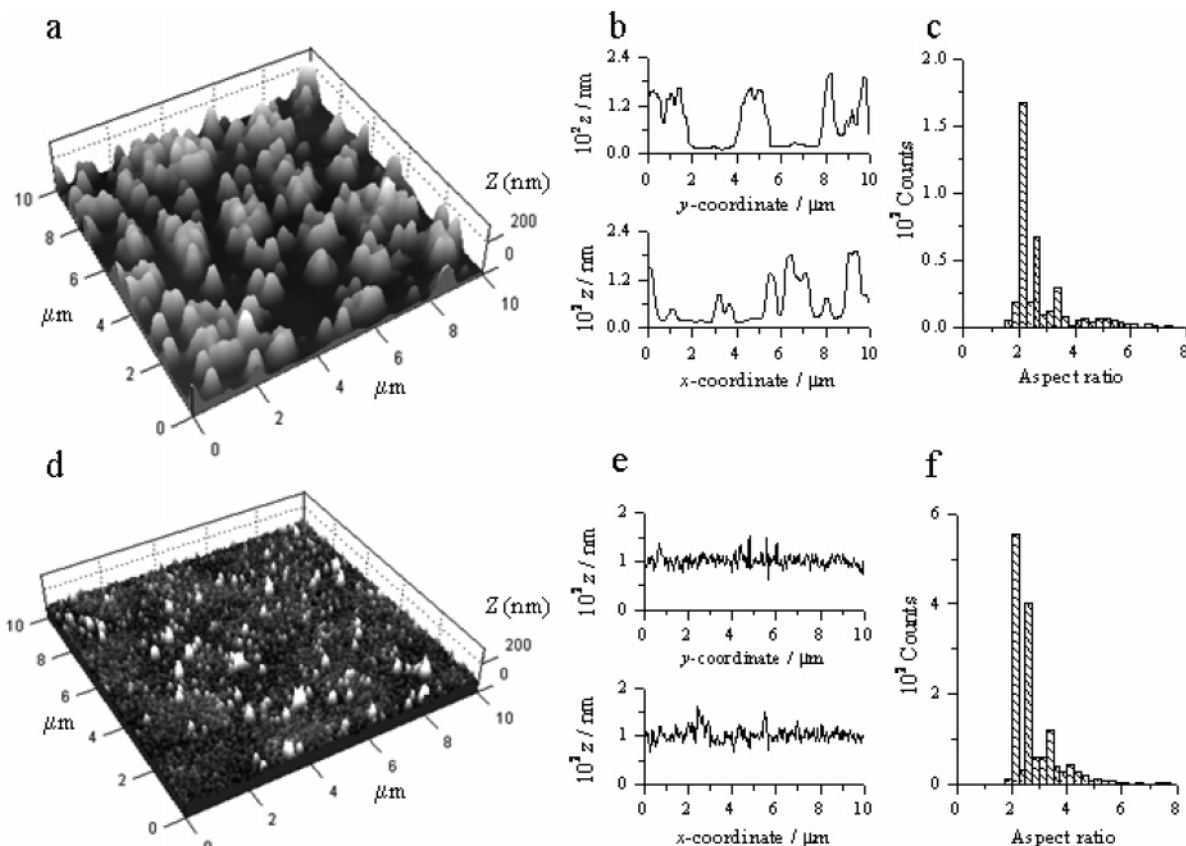
Figure 5. AFM images ($10 \times 10\ \mu m^2$) of WEIII ($q_{Pt} = 19\ mC/cm^2$) (a) and ($q_{Pt} = 192\ mC/cm^2$) (d). The corresponding cross-section analysis in the x and y directions is shown in b and e, and aspect ratio distribution functions for the mesoscale topography are depicted in c and f, respectively.

Table 2. Statistical Parameters Derived from the Roughness Analysis of AFM Images[a]

	WEI-19	WEI-96	WEII-19	WEII-96	WEII-192	WEIII-19	WEIII-96	WEIII-192
Sq nm	24.2	39.8	46.0	38.7	121	51	22.4	17.5
Ssk	0.316	0.729	0.366	−0.921	−0.250	0.901	0.367	1.97
Sku	3.28	2.55	2.19	3.67	1.82	2.69	2.81	12.9
Sti	0.810	0.261	0.285	0.640	0.721	0.608	0.761	0.556
Spk nm	30.7	71.3	50.0	30.6	77.6	108	26.7	40.3
Sk nm	60.3	67.8	110	66.7	267	60.4	59.9	31.5
Svk nm	17.0	3.0	15.8	73.1	134	5.11	10.9	13.4
D_f	2.77 ± 0.05	2.77 ± 0.05	2.73 ± 0.05	2.85 ± 0.05	2.90 ± 0.05	2.92 ± 0.05	2.99 ± 0.05	2.71 ± 0.05
P	0.34 ± 0.03	0.42 ± 0.03	0.11 ± 0.03	0.20 ± 0.03	0.37 ± 0.03	0.16 ± 0.03		0.20 ± 0.03
$A_H\ cm^2$	0.30	1.80	0.40	1.60	3.30	0.30	2.50	2.80

[a] Root-mean-square height in the z direction (Sq), the skewedness (Ssk), the Kurtosis parameter (Sku), the texture parameter (Sti), Abbott curve parameters (Sk, Spk, and Svk), the fractal dimension (D_f), the roughness exponent (p), and the real surface area (A_H). Numbers in WE column headings refer to the platinum loading of WEs.

parameters: Sk, which is related to the fraction of heights emerging from the plateau with minimum slope including 40% heights (core); Spk, which provides an estimation of the number of protrusions; and Svk, the number of valleys with respect to the core. (vii) The fractal dimension D_f.

Statistical parameters derived from the roughness analysis on the mesoscale are assembled in Table 2. For WEI, when q_{Pt} is increased from 19 to 96 mC cm^{-2}, there is a slight increase in the value of Sq, whereas the reverse effect occurs for WEII (Figures 3 and 4). However, for $q_{Pt} = 192$ mC cm^{-2} Sq increases rather abruptly. The small value of Sq for $q_{Pt} = 96$ mC cm^{-2} accounts for the increasing influence of coalescence phenomena. For WEIII, the value of Sq decreases as q_{Pt} is increased. Seemingly, Sq approaches a limiting value of about 17 for $q_{Pt} = 192$ mC cm^{-2}. This may imply a counterbalance between surface atom mobility at upper lattice layers and coalescence phenomena. As far as skewedness is concerned, for WEI the

value of Ssk increases positively with q_{Pt}. In contrast to WEI, for WEII, when q_{Pt} is increased from 19 to 192 mC cm^{-2}, an abrupt change from a positive to a negative value of Ssk is observed. This is an indication that for WEI there are topography transitions from valleys to peaked heights, whereas the reverse occurs for WEII. For WEIII with $q_{Pt} = 19$ mC cm^{-2}, protruding spikes a few nanometers in height play a relevant role in the characteristics of the surface, whereas for $q_{Pt} = 192$ mC cm^{-2} the large value of Ssk does not permit a characterization of the quality of the surface.[43] Thus, for the largest q_{Pt} the formation of valleys should be assisted by coalescence phenomena.

The value of Sku is in the range of 1.8 to 3.5 for all WEs, except for WEIII with $q_{Pt} > 100$ mC cm^{-2}. All values of Sti are lower than 1, as expected for anisotropic deposits. The largest value of Sti comes from WEI ($q_{Pt} = 19$ mC cm^{-2}), and the lowest ones result from WEI ($q_{Pt} = 96$ mC cm^{-2}) and WEII ($q_{Pt} = 19$ mC cm^{-2}). The parameters derived from the cumulative
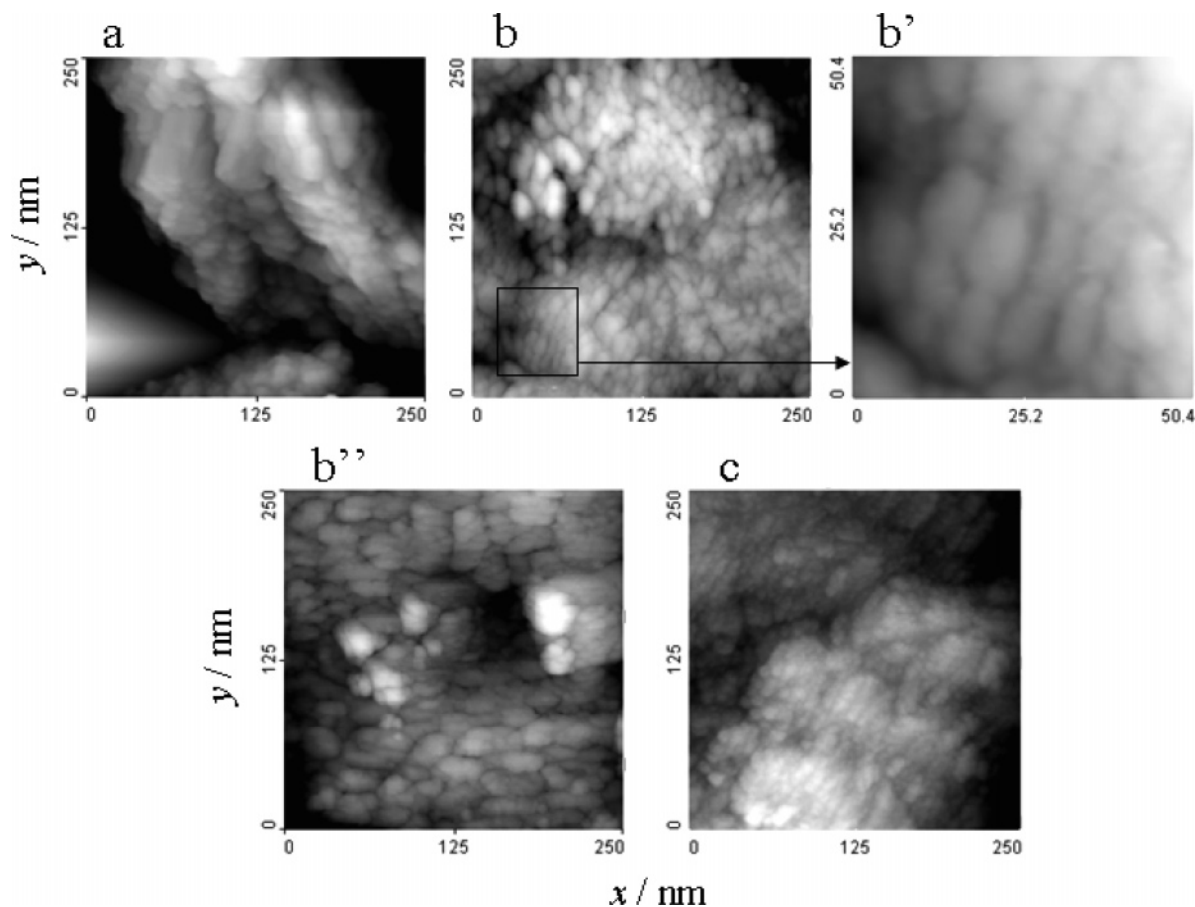
Figure 6. STM image (250 × 250 nm²). (a) WEI (q_{Pt} = 19 mC cm⁻²); (b) WEII (q_{Pt} = 19 mC cm⁻²); (b′) Close-up view (50.4 × 50.4 nm²) showing ordered domains of aligned clusters; (b″) WEII (q_{Pt} = 96 mC cm⁻²); (c) WEIII (q_{Pt} = 19 mC cm⁻²).

probability distribution function (Sk, Spk, and Svk) permit a more detailed description of the changes in surface morphology at different q_{Pt} values. Thus, for WEI, the Spk/Svk ratio increases with q_{Pt} and demonstrates an increase in the fraction of the surface associated with protrusions. The reverse effect is produced for WEII as result of the contribution of coalescence phenomena. The effect is the smoothing of peaks and the dominant contribution of valleys to the topography. For WEIII, no clear trend can be derived from the Spk/Svk ratio, although Svk increases with q_{Pt} as valleys become the dominant features.

The data assembled in Table 2 provide quantitative support to evaluate the contribution of protrusions and valleys to the topography. It is clear that except for WEI at the lowest q_{Pt}, the rest of the WEs at lower q_{Pt} protrusions and peaked heights dominate the surface morphology, whereas valleys prevail for higher q_{Pt} values. However, the data reveal the complexity of the topography that can be described in terms of a structure that lies between an ordered and a completely disordered structure. This is consistent with the fractal behavior of the electrodeposits.

The statistical analysis that depends on the pixel size always provides a real surface value that is smaller than that resulting from A_H. To surmount these limitations, we attempted to correlate the roughness of the electrodeposit in terms of A_H with the exponent (p) resulting from the slope of the log(local Sq) versus log(system size) plot, as an extension of the dynamic scaling theory[44] to a nonsaturated interface. Values of p and A_H, as expected, fit the proportionality $A_H \propto p$ (Table 2).

3.2. Surface Characterization of WE by STM. To characterize further details of the WE topography on the nanometer level, STM images at different scales were obtained (Figure 6), although it should be noted that the atomic lattice resolution for these rough surfaces, under the present experimental conditions, is not feasible.

The STM image (250 × 250 nm²) of WEI (q_{Pt} = 19 mC cm⁻²) (Figure 6a) is made of a large number of aggregates of clusters that look like pyramids (i.e., the electrodeposit is to a large extent faceted, suggesting the possible contribution of (111) facets). The cross-section analysis and the length and width distribution function (Figure 7a–c, I) show irregular rows of anisotropic clusters, with their average aspect ratio being 2.98.

The STM images (250 × 250 nm²) for WEII (q_{Pt} = 19 mC cm⁻²) (Figure 6b) reveal that each platinum aggregate consists of irregular clusters about 5–20 nm in average length and a few atoms in height. A quasi-periodic linear distribution of these clusters along the x and y directions can be deduced from both the cross-section analysis (Figure 7a–c, II) and the close-up view of the domain of the image (Figure 6b′). The cross sections are randomly modulated by surface defects that appear as both spikes of a few atoms either in height or depth and short steps at the surfaces of clusters (Figure 7a–c,II).

STM images resulting from WEII (q_{Pt} = 96 mC cm⁻²) (Figure 6b″) exhibit domains of pebblelike clusters rather uniformly distributed and some valleys and protrusions. Roughly the same behavior is observed for q_{Pt} = 192 mC cm⁻². In this case, the pebblelike structure resembles the structure that has been observed for platinum surfaces activated by cyclic perturbations.[45] The aspect ratio derived from STM data changes from 3.30 for q_{Pt}

(44) Barabási, A. L.; Stanley, H. E. *Fractal Concepts in Surface Science*; Cambridge University Press: Cambridge, England, 1995.
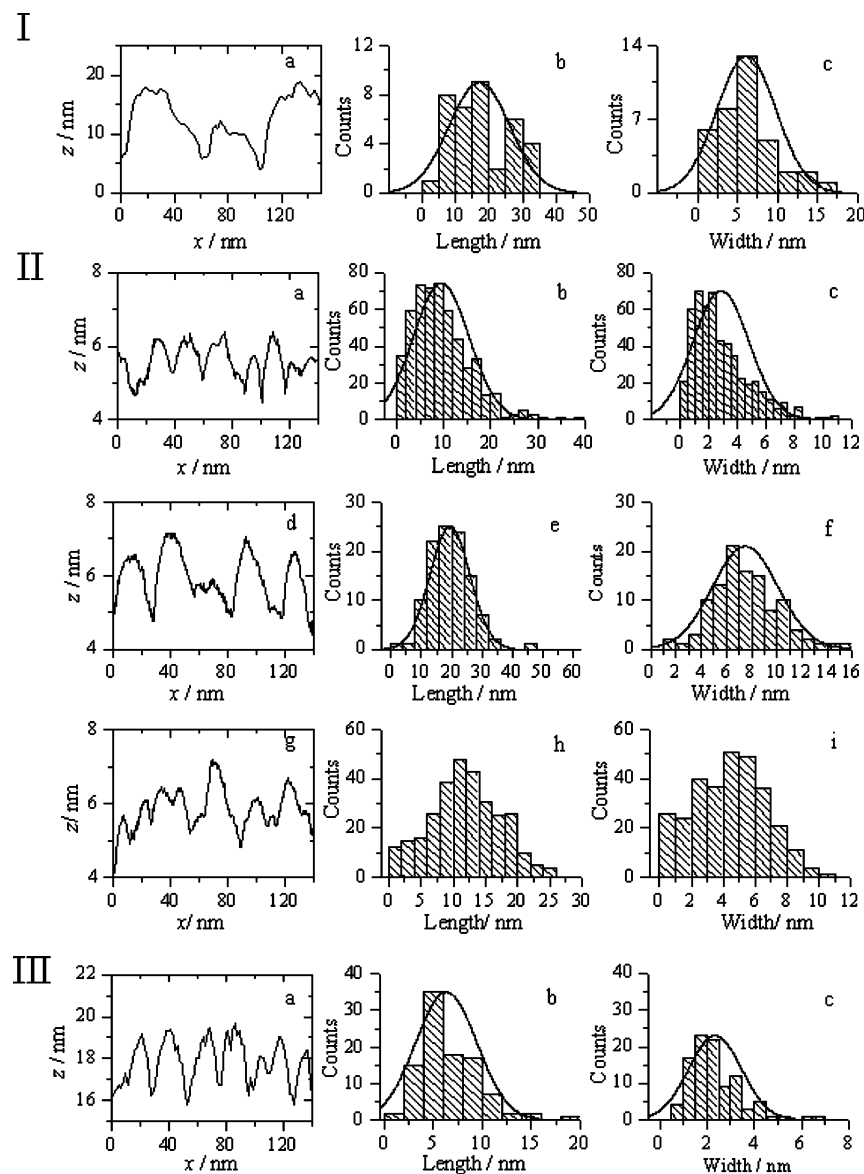
Figure 7. Cross-section analysis and length and width distribution functions derived from STM imaging. (I) WEI ($q_{Pt} = 19$ mC/cm^2) cross-section analysis (a); length (b) and width (c) distribution functions. (II) WEII ($q_{Pt} = 19$ mC/cm^2) (a), ($Q_{Pt} = 96$ mC/cm^2) (d), and ($Q_{Pt} = 192$ mC/cm^2) (g) cross sections; length (b, e, and h) and width (c, f, and i) distribution functions. (III) WEII ($q_{Pt} = 19$ mC/cm^2) cross section (a); length (b) and width (c) distribution functions.

$= 19$ mC cm^{-2}, to 2.55 for $q_{Pt} = 96$ mC cm^{-2}, and to 2.68 for $q_{Pt} = 192$ mC cm^{-2} (Figure 7a−i, II). This aspect ratio change is accompanied by the disappearance of the cluster periodicity on the nanometer scale.

The STM image (250×250 nm^2) of WEIII (Figure 6c) shows aggregates consisting of flat clusters smaller than 10 nm and a few atoms in height that tend to acquire a triangular shape. Some of these clusters are packed to constitute domains with a quasi-parallel arrangement, and others tend to form grape-bunch-like aggregates. The cross section is shown in Figure 7a, III; the aspect ratio is almost the same as that of WEII ($q_{Pt} = 192$ mC cm^{-2}); the length and width distribution functions fit reasonable Gaussian behavior (Figure 7b and c, III).

The average cluster width and length and their variances are assembled in Table 1. For WEII ($q_{Pt} = 96$ mC cm^{-2}), the smallest aspect ratio and the largest cluster size are obtained, whereas the

maximum aspect ratio results from WEII ($q_{Pt} = 19$ mC cm^{-2}). For WEII at different q_{Pt} values, the variances in length and width are 6 ± 0.6 and 2.3 ± 0.4 nm, respectively. These values are intermediate between those found for WEI and WEIII.

3.3. Electrochemical Characterization of WEs: H-Atom Electrosorption. The H-atom electrosorption voltammograms run with WEs in aqueous 1 M sulfuric acid (Figure 8) show cathodic and anodic current contributions in the range of 0.05 to 0.30 V. The anodic-to-cathodic charge ratio derived from the integration of these voltammograms is close to 1, irrespective of the WE preparation procedure.

A typical voltammogram at WEI (Figure 8a) run in the positive-going potential scan shows an anodic current peak at 0.08 V and a small anodic hump at higher E and increasing cathodic current with humps on the reverse scan. A comparable voltammogram from WEII (Figure 8b) shows a broad anodic current peak at 0.150 V with a small hump at ca. 0.25 V in the positive-going potential scan and a continuous cathodic current increase from 0.30 to 0.05 V in the reverse scan. The voltammogram from
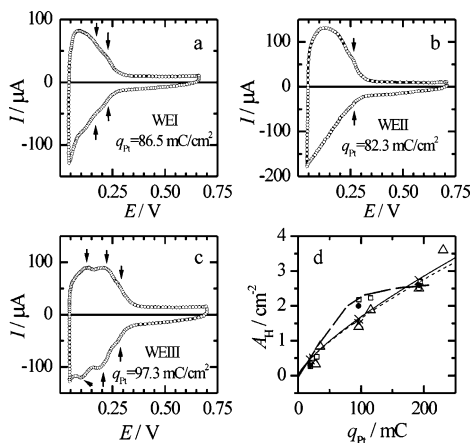
(45) Zubimendi, J. L.; Andreasen, G.; Triaca, W. E. *Electrochim. Acta* **1995**, *40*, 1305.

Figure 8. H-adatom electrosorption voltammograms run at 0.050 V s^{-1} in 1 M sulfuric acid. (a) WEI, (b) WEII, and (c) WEIII (21 $\leq q_{Pt} \leq$ 26 mC/cm²). (d) A_H vs Q_{Pt} plots for WEI ($\triangle$), WEII ($\times$), and WEIII ($\square$). Traces describe the behavior referred to in the text. (●) Data calculated from AFM data as indicated in the text.

WEIII (Figure 8c) displays cathodic and anodic current contributions in the range of 0.05 to 0.35 V and three small pairs of conjugated current peaks (arrows in Figure 8).

WE electrochemical data also show that A_H, the real platinum electrodeposit area, increases with q_{Pt}. For WEIs and WEIIs, the proportionality $A_H \propto q_{Pt}^b$ is fulfilled (Figure 8d), where $b = 0.75 \pm 0.13$ (i.e., the lower dA_H/dq_{Pt}, the larger q_{Pt}). For WEIIIs, the value of A_H increases almost linearly with q_{Pt} only for small values of q_{Pt}, whereas for $q_{Pt} = 96$ mC cm^{-2} A_H tends to reach a saturation value. This behavior appears to be consistent with $D_f \cong 3$ resulting from WEIIIs at low q_{Pt} (Table 2). The corresponding voltammogram appears to be similar to that resulting from a platinum single-crystal microsphere in 0.5 M sulfuric acid after it has been square wave potential cycled in a platinum plating solution.[46]

Otherwise, the voltammograms for WEI and WEII (Figure 8a and b) show the rapid disappearance of the H-adatom voltammetric charge at 0.275 V, and in the voltammogram for WEIII, the same behavior is seen at 0.300 V. These potentials are very close to the potentials of zero total charge (pztc) that have recently been reported for platinum nanoparticles of mean diameters in the range of a few nanometers.[15]

4. Discussion

4.1. Some Remarks on the Platinum/HOPG System. *4.1.1. Platinum Electrodeposition on HOPG.* Conventional polycrystalline platinum electrodeposition on HOPG from aqueous hexachloroplatinic acid is a convective diffusion-controlled process that involves two main stages, namely, the formation of a first discontinuous film stage and the later continuous film stage. In agreement with this description, surface images of WEs resulting from low values of q_{Pt} show three main domains: (i) bare HOPG, (ii) platinum-covered HOPG, and (iii) the HOPG/platinum contact zone.[45−48] Conversely, for large q_{Pt} values this third domain is practically suppressed. In any case, the WE heterogeneous surface implies domains of aggregates and clusters of different size, shape, crystallography, and degree of disorder of the ensemble of clusters and aggregates.

In fact, sequential STM imaging for the early stage of growth for low q_{Pt} and low cathodic overvoltage show rounded clusters that are formed at substrate defect sites, particularly at step edges,

according to a Volmer-type nucleation and growth mechanism.[40,41,49] These clusters first tend to form rows aligned in well-defined directions and further yield orderly 3D structures leading to step decoration. Throughout the early stages of growth, platinum atoms produced by discharging complex platinum ions from the solution, either at the HOPG surface or at platinum aggregates or clusters, arrive at aggregate or cluster edges both by surface diffusion on HOPG and from platinum aggregates or cluster tops via cascade surface diffusion. When the central core diameter exceeds a critical value of about 10−20 nm, cluster coalescence begins to be observed (Figure 6). Later, the growth and coalescence of neighbor clusters produce aggregates with an incipient faceting[10,45] that depends on the operating conditions.

Aggregate coarsening and coalescence are evident when the aggregate diameter and height exceed 20 and 4 to 5 nm, respectively. Then, they result in the filling out of inter-aggregate spaces and valleys, without a significant increase in either the maximum aggregate height or lateral dimension. Finally, at advanced stages of growth the filling of inter-aggregate spaces and aggregate overlapping lead to the development of faceted, compact platinum patterns. Again, the potential modulation included in the preparation procedure of WEs makes the diffusion-controlled electrodeposition and the transport of adatoms along the deposit surface faster, resulting in smooth electrofaceted, stress-relieved deposits. In fact, as q_{Pt} and the cathodic overvoltage are increased, compact platinum stepped crystals with flat terraces are formed.[45]

The electrochemical faceting of platinum can be followed via the height ratio of the conjugated current peaks of weakly and strongly bound H-adatoms that appear in the range of 0.1 to 0.3 V.[14,35] This effect is usually accompanied by an increase in the contribution of (110)-type facets.[35,46] The electrochemical faceting commences by a reordering of surface atoms induced by changes in the charge distribution at the electrical double layer and H-atom electrosorption processes. The overall process yields first a nanofaceting on the 10 nm scale or thereabouts and later macrofaceting consisting of crystallites on the order of 1 μm. Then, the topography appears as a weakly disordered stepped surface with a roughness factor that is usually lower than 3. The contribution of roughening can be determined by the enhancement of the overall H-atom electrosorption charge[13,20]

4.1.2. Platinum Electrodeposition on HOPG under Potential Modulation. The potential modulation increases the rate of convective diffusion of the complex platinum ion in solution as the average thickness of the diffusion layer decreases with the reciprocal of $f^{1/2}$ (refs 50 and 51) and the surface relaxation processes that play a relevant role in determining the surface morphology.

Let us first consider the main surface processes involved in the preparation of WEI and WEII in which H-adatoms are involved. For WEIs, the repetitive symmetric triangular potential modulation implies, for each cycle, a residence time for the cathodic (τ_c) and anodic (τ_a) half-cycles of $\tau_c = \tau_a = 10$ s and for WEIIs a residence time of $\tau_c = \tau = 10$ s (i.e., a time that is sufficiently long to favor the participation of platinum surface atom (or small cluster) relaxation processes[41]). However, the contribution of these processes depends on whether the cathodic or the anodic reaction is considered. As can be concluded from

(46) Egli, W. A.; Visintin, A.; Triaca, W. E.; Arvia, A. J. *Appl. Surf. Sci.* **1993**, *68*, 583.

(47) Walden, M.; Lai, X.; Goodman, D. M. *Science* **1998**, *281*, 1647.
(48) Bell, A. T. *Science* **2003**, *299*, 1685.
(49) Lorenz, H. J.; Plieth, W., Eds. *Electrochemical Nanotechnology: In Situ Local Probe Techniques at Electrochemical Interfaces*; Wiley-VCH: Weinheim, Germany, 1998.
(50) Despic, A. R.; Popov, K. I. *J. Appl. Electrochem.* **1971**, *1*, 275.
(51) Podestá, J. J.; Paús, G. F.; Arvia, A. J. *Electrochim. Acta* **1974**, *19*, 583.

the A_H versus q_{Pt} plot (Figure 8d) for WEIs and WEIIs with small q_{Pt} values, the influence of the potential routine is reflected in the values of the parameters assembled in Table 2, particularly the value of Sq. The average surface displacement of adatoms or clusters of a few adatoms can be estimated from the expression $\langle \Delta x \rangle \cong (D_s \tau)^{1/2}$, where D_s is the surface diffusion coefficient for platinum, either atoms or small clusters. Thus, for the value of τ of the modulating signals and by taking $D_s \cong 10^{-14}$ cm^2 s^{-1} (ref 41) as the average surface diffusion coefficient over the range of ΔE covered by the experiments,[41,52] $\langle \Delta x \rangle = 7 \times 10^{-7}$ cm is obtained. Then, the surface diffusion of platinum atoms or small clusters and the presence of H-adatoms should determine the topography of these electrodes, particularly for low values of q_{Pt}.

The convective diffusion process is greatly enhanced for the preparation of WEIII at $f = 5000$ Hz, whereas the surface relaxation processes described above become less important in comparison to the contribution of phonon dispersion to a reordering of the atomic lattice at the electrode/solution interface. This contribution involves only longitudinal waves producing atom displacements to new equilibrium positions in the lattice, which have been predicted by using the parameters of the periodic signals.[42,53]

4.2. WE Surface Morphology. The description of WE surface morphology depends on the yardstick size. In this respect, the cross-section analysis of AFM and STM images permits the recognition of microroughness at the level of aggregate size and nanoroughness of clusters forming aggregates, respectively. Grain analysis data resulting from AFM and STM images allowed us to characterize the shape of aggregates and clusters, respectively, and to describe the topography of the electrodeposits on different scales. The parameters assembled in Table 1 are averaged values from at least five images. It is worth noting that a similar aspect ratio is derived from AFM and STM data.

The topography of the electrodeposits can be quantitatively described along with its evolution with q_{Pt} considering morphological parameters resulting from AFM and STM images all together instead of considering each one independently because this might introduce some ambiguity. For example, rough surfaces consisting of aggregates and clusters of different sizes and shapes would have the same Sq values (Table 2). Thus, low values of Ssk (also negative) and large values of Svk from the Abbott curve (relative to Sk and Spk) indicate a surface with a height distribution function comprising a large number of heights below the average value (i.e., a large fraction of the profile associated with valleys). In contrast, for large values of Ssk and Spk (relative to values of Sk and Svk), the topography is dominated by peaks (section 3.1.4). As q_{pt} is changed, a quantitative correlation of the topography features with Ssk and Spk can be obtained. Large values of Sk are associated with the formation of large mounds, as in the case of WEIIs with large q_{Pt} values. For WEIII, no mounds are formed, but small aggregates with a peaked shape are obtained from the relatively high values of Spk. Large values of Sk can be ascribed to the disorder of the surface topography, in agreement with the value of D_f. Skw values and the variances in height and width, which take into account the broadness of the distribution of data around the average values, increase for samples with highly disordered structures.

The magnitude of the anisotropy is quantitatively described by the aspect ratio and values of Sti. The greater the former and the lower the latter, the larger the anisotropy. Particularly for
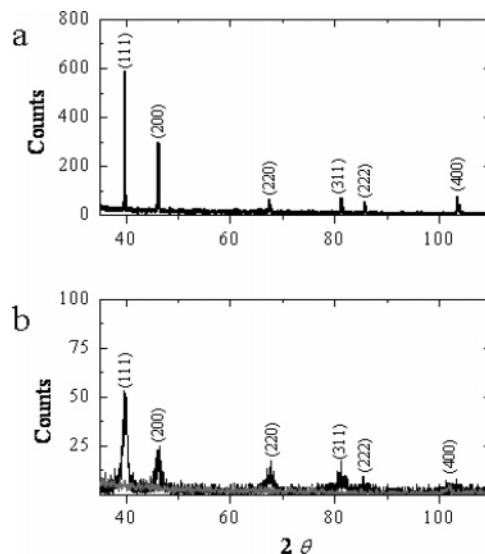

Figure 9. (a) X-ray diffraction patterns. (a) Polycrystalline platinum sample (blank). (b) WEI platinum electrodeposit ($q_{Pt} = 192$ mC cm^{-2}). The HOPG blank is depicted in the gray traces.

WEI and WEII, the lower the q_{Pt}, the greater the anisotropy. The aspect ratio and Sti values present the greatest variation for WEI and WEII. In contrast, for WEIIIs they remain almost constant.

The consistency of the size parameters derived from AFM images can be tested by considering spherical aggregates with an average diameter size (Table 1). Accordingly, their number density can be estimated by dividing the total area of the sample by the average transversal area of the aggregates (Table 1, first row). For WEs with low q_{Pt} values, the total surface area of the spheres is corrected by the partial HOPG surface coverage and by a factor to adjust the calculated and experimental values of q_{Pt}. Despite the rawness of the model in which no roughness factor correction is made, calculated results, which are depicted in Figure 8d, are comparable to the experimental data estimated from A_H.

4.3. WE Polycrystalline Surface and H-Adatom Voltammetric Response. The relationship between the polycrystalline surface of WEs and the features of their H-adatom voltammograms can be tentatively approached starting from the comparison of XRD data (Figure 9), which show that the simultaneous platinum electrodeposition under potential modulation increases the number density of high-Miller-index facets with relevant contributions of (110), (100), and (200) planes, such as (210) = 1(100) + 2(110), (311) = 2(100) + 1(111), and (331) = 2(110) + 1(100).[35]

The broad voltammetric current peaks in the range of 0.05−0.45 V described for WEs in section 3.3.1 can be related to H-atom electrosorption at facets where the coordination number (CN) of the platinum atom to the lattice is smaller than 9.[35] Thus, the number of current peaks appearing in the range 0.1 to 0.3 V can be assigned to facets involving the (110) and (100) plane, whereas a smaller current contribution around 0.4 V peaks can be related to facets with the contribution of the (111) plane. This analysis is consistent with the assignment of H-adatom current peaks for different crystal faces with 7.5 ± 2.8 nm mean diameter platinum particles in 0.5 M sulfuric acid at 0.02 V s^{-1} that has recently been reported.[54] In this case, the current peak at 0.125 V has been assigned to Pt(110), that at 0.27 V, to Pt(100), that at 0.36 V, to (100) terraces, and that at 0.5 V, to (111) terraces.

(52) Hidalgo, M.; Marcos, M. L.; González Velasco, J. *Appl. Phys. Lett.* **1995**, *67*, 1486.
(53) Zinola, C. F.; Bello, C. *J. Colloid Interface Sci.* **2003**, *258*, 259.

(54) . Solla-Guillón, J.; Vidal-Iglesias, F. J.; Rodríguez, P.; Herrero, E.; Feliú, J. M.; Clavilier, J.; Aldaz, A. *J. Phys. Chem. B* **2004**, *108*, 13573.

Therefore, from the above discussion it is reasonable to explain the displacement of the maximum H-adatom charge toward lower potentials for WEs (Figure 8).

Further support for the above conclusions results from the estimation of the relative specific free energy $\gamma(hkl)$ of any (hkl) pole located in the fundamental fcc crystallographic triangle with the equation[55]

$$\gamma(hkl) = \left[\frac{f(N) A_r(111)}{A_g(hkl)}\right]\gamma(111) \quad (1)$$

in which $\gamma(111)$ and $A_r(111)$ are the surface free energy and the geometric surface area of the (111) pole taken as reference, respectively; $A_g(hkl)$ is the real geometric area of the (hkl) pole made of arrangements of (111), (100), and (110) fundamental microfacets; and $f(N)$ is a correction factor accounting for how far the surface structure is from that of the ideal (111) atomic fcc arrangement.[56,57] Thus, from eq 1, taking $\gamma(111)/\gamma(111) = 1$, the following relative surface free-energy values of different fcc packings are $\gamma(100)/\gamma(111) = 1.151$; $\gamma(110)/\gamma(111) = 1.228$; $\gamma(311)/\gamma(111) = 1.216$; and $\gamma(210)/\gamma(111) = 1.284$. These data for the fcc crystallographic structure depend on the orientation of each facet and the coordination number of platinum atoms in the lattice. They indicate that the electrofaceting techniques favor a polycrystalline topography of aggregates and clusters with a greater contribution of high-Miller-index facets introducing the dependence of the H-adatom−platinum interaction energy on the different platinum facets that is reflected in the H-adatom voltammograms.

5. Conclusions

The electrodeposition of platinum on HOPG under potential modulation offers the possibility of producing metal surfaces consisting of aggregates on the micrometer scale made of nanometer-sized clusters. The grain topography depends on the modulating potential routine and the platinum electrodeposition charge.

The topography of WEs and its dependence on the electrodeposition charge can be quantitatively described by a set of parameters derived from the statistical grain and roughness analyses of AFM and STM images. These data provide surface areas of WEs that are comparable to those obtained from the voltammetric hydrogen atom electrosorption charge. The electrochemical roughness also correlates with the exponent derived from the log(local Sq) versus log(system size) plot, as an extension of the scaling theory under nonequilibrium.

The WE heterogeneous surfaces consist of domains covered by high-index platinum facets and bare HOPG domains for low electrodeposition charges, whereas for high coverage only the former type of domain exists. For low coverage, a third domain involving the platinum/HOPG contact zone deserves attention because of its contribution to surface heterogeneity.

The topography of WEs can then be described as a surface structure intermediate between a well-ordered (Euclidean) and a disordered (fractal) atomic lattice arrangement. Accordingly, the physicochemical properties of the electrode surface, among them the electronic energy distribution, should depend, to some extent, on the fractal geometry.

WE surfaces exhibit a dominant contribution for weakly bound H-adatom electrosorption in aqueous sulfuric acid. The intensity and location of the H-adatom voltammetric peaks can be explained in terms of the enhancement of the contribution of high-Miller-index plane facets. The dependence of the H-adatom-platinum atom interaction energy on the coordination number of the platinum atom in the lattice can also explain the role played by H-atoms in the electrofaceting and roughening of platinum.

In the absence of H-adatom formation, smooth electrofaceting is produced. In this case, the H-adatom voltammetric response is consistent with an increasing participation of (111) planes in high-Miller-index stepped facets.

(55) Canullo, J. C.; Tignanelli, H. L.; Plastino, A.; Arvia, A. J. *Langmuir* **1991**, *7*, 1269.
(56) Van Hove, M. A.; Somorjai, G. A. *Surf. Sci.* **1980**, *92*, 489.
(57) Hamelin, A.; Vitanov, T.; Svastyanov, E.; Popov, A. *J. Electroanal. Chem.* **1983**, *145*, 225.